communications materials

Article

https://doi.org/10.1038/s43246-024-00635-9

Ideal spin-orbit-free Dirac semimetal and diverse topological transitions in Y_8CoIn_3 family

Manabu Sato [1], Juba Bouaziz [2], Shuntaro Sumita [3,4,5], Shingo Kobayashi[6], Ikuma Tateishi[6], Stefan Blügel [2], Akira Furusaki [5,6] & Motoaki Hirayama [1,6]

Topological semimetals, known for their intriguing properties arising from band degeneracies, have garnered significant attention. However, the discovery of a material realization and the detailed characterization of spinless Dirac semimetals have not yet been accomplished. Here, we propose from first-principles calculations that the RE_8CoX_3 group (RE = rare earth elements, X = Al, Ga, or In) contains ideal spinless Dirac semimetals whose Fermi surfaces are fourfold degenerate band-crossing points (without including spin degeneracy). Despite the lack of space inversion symmetry in these materials, Dirac points are formed on the rotation-symmetry axis due to accidental degeneracies of two bands corresponding to different 2-dimensional irreducible representations of the C_{6v} group. We also investigate, through first-principles calculations and effective model analysis, various phase transitions caused by lattice distortion or elemental substitutions from the Dirac semimetal phase to distinct topological semimetallic phases such as nonmagnetic linked-nodal-line and Weyl semimetals (characterized by the second Stiefel–Whitney class) and ferromagnetic Weyl semimetals.

Topological semimetals are a fascinating group of materials with degeneracies between valence and conduction bands that exhibit intriguing properties in the bulk and at the surface, e.g., due to interference effects between the electronic states around the degeneracy points[1]. There exist various types of topological semimetals in real materials including Weyl[2–6], Dirac[7–14], and nodal-line semimetals[15–22], for spinless and spinful systems. Here spinless systems refer to electron systems without spin-orbit couplings (SOC), where the spin degrees of freedom can be omitted due to the spin degeneracy, while spinful systems have the SOC, which breaks SU(2) spin rotation symmetry. Although all real materials have finite SOC, it is reasonable to first discuss the topology as spinless systems and then examine the effect of the SOC when studying materials with weak SOC. This is because there are topological invariants that take nontrivial values only in systems without the SOC, such as the quantized Berry phase protected by a combination of space inversion and time reversal symmetry[23–25]. Hereafter we will disregard the spin degrees of freedom when counting the degree of degeneracy in spinless systems.

The recent development of the representation theory of electronic energy bands, such as symmetry-based indicators[26,27] and topological quantum chemistry[28], has enabled the exhaustive search over crystal databases for topological materials[29–34]. Nevertheless, the comprehensive classification and detailed characterization of topological semimetals are still lacking. For example, no material realization of spinless Dirac semimetals with a quadruple degenerate point between the valence and conduction bands has been discovered to the best of our knowledge. The difference between the spinless Dirac semimetal and other well-known topological semimetals with quadruple degeneracy is given in Supplementary Note 1. In fact, the irreducible representations (irreps) of valence bands at high symmetry points alone cannot tell us whether the material in question is an ideal semimetal without superfluous Fermi surfaces of finite area, while they can determine the presence of nodes and their degree of degeneracy[29–35]. Moreover, for spinless systems, there is currently no guiding principle for the realization of band inversion, which is essential for the design of topological insulators and topological semimetals, in contrast to the spinful systems, where the band inversion can be achieved by strong SOC. Thus, the study of spinless topological materials lags behind that of spinful ones. In the search for material realizations of the symmetry-protected Dirac semimetals, the representation theory of space groups is essential. In spinful systems, there are two distinct classes of Dirac semimetals[1,36,37]. In one class of Dirac semimetals, a pair of Dirac points is formed due to an accidental

[1]Department of Applied Physics, The University of Tokyo, Bunkyo, Japan. [2]Peter Grünberg Institut and Institute for Advanced Simulation, Forschungszentrum Jülich and JARA, Jülich, Germany. [3]Department of Basic Science, The University of Tokyo, Meguro, Japan. [4]Komaba Institute for Science, The University of Tokyo, Meguro, Japan. [5]Condensed Matter Theory Laboratory, RIKEN CPR, Wako, Japan. [6]RIKEN Center for Emergent Matter Science, Wako, Japan.
e-mail: hirayama@ap.t.u-tokyo.ac.jp

band crossing of two different 2-dimensional irreps on a high-symmetry line, as seen in Na_3Bi[8,9] and Cd_3As_2[10–14]. In the second class of Dirac semimetals with nonsymmorphic symmetry, such as β-BiO_2[7], a Dirac point appears as a 4-dimensional irrep at a high-symmetry point on the boundary of the Brillouin zone (BZ). These two classes of Dirac semimetals are also expected to exist in spinless systems, and the space groups that can realize each class are listed in ref. 38. We note that the study of spinful Dirac semimetals is carried out using double-valued representations, while the study of spinless Dirac semimetals is based on single-valued representations. This corresponds to the fact that a spinless Dirac point does not consist of the spin degrees of freedom, but only of the orbital (pseudospin) degrees of freedom. In other words, in spinless Dirac semimetals, eight bands including the spin degrees of freedom form the degeneracy, which clearly distinguishes spinless Dirac semimetals from already well-studied spinful Dirac semimetals.

In this paper, we study the first class of spinless Dirac semimetals and their material realization. We focus on the space groups with C_{6v} symmetry that accommodates two 2-dimensional irreps along a high symmetry line in the BZ. In addition to the space group considerations, we utilize the chemical bonding perspective to design ideal Dirac semimetals. We choose elements with similar electronegativity that form covalent bonds, which we expect to result in the reduction of the density of states (DOS) at the Fermi energy. Our study reveals that materials within the RE_8CoX_3 group (RE = rare earth elements, X = Al, Ga, or In) exhibit the spinless Dirac semimetal phase with nontrivial topological properties. These materials have C_{6v} symmetry on the high symmetry line in the BZ. We will begin by discussing these materials' crystal structure and their symmetry. Taking Y_8CoIn_3 as an example, we will present the bulk electronic structure and the characterization of its topology, and describe the surface states and their correspondence to the bulk topological invariant. Next, we will show the diverse topological phase transitions caused by symmetry reductions in the target materials, from the Dirac semimetallic phase to nodal-line and Weyl semimetallic phases characterized by the second Stiefel–Whitney (SW) class. Finally, we will consider the substitution of rare earth elements to introduce strong SOC and discuss possible magnetic properties.

Results

Electronic band structure

Among the ternary compounds RE_8CoX_3 (RE = rare earth elements, X = Al, Ga, or In), the experimentally synthesized compounds all show a hexagonal crystal structure with the nonsymmorphic space group $P6_3mc$ (no. 186)[39–41]. This structure lacks space inversion symmetry and has a polarization along the c-axis. Figure 1 shows the crystal structure of Y_8CoIn_3[40], where the measured lattice constants are $a = b = 10.3678$ Å and $c = 7.0069$ Å. The crystal structure is three-dimensional and the composition is primarily made up of Y elements. The space group has a sixfold screw symmetry around the z-axis $\{C_{6z}|00\frac{1}{2}\}$, a mirror symmetry with respect to the yz-plane $\{M_x|000\}$, and a glide symmetry with respect to the zx-plane $\{M_y|00\frac{1}{2}\}$, where the z direction is taken to be along the c-axis. As a result, the little co-group C_{6v} is formed along the k_z-axis (Γ-A line in the BZ).

Figure 2a shows the electronic band structure of Y_8CoIn_3 calculated in the absence of the SOC, with the corresponding bulk BZ shown in Fig. 2b. Clearly, Y_8CoIn_3 is an ideal semimetal with the band crossing along the Γ-A line. The Fermi surface of this semimetal consists of two Fermi points on the k_z-axis that are related by time-reversal symmetry. This band structure is well reproduced by the Korringa–Kohn–Rostoker (KKR) method (see Supplementary Note 2). The DOS shown in Fig. 2c suggests that the bands near the Fermi level originate mainly from the Y 4d orbitals, the Co 3d orbitals, and the In 5p orbitals. We note that the Y atoms occupy four Wyckoff positions, and all of them contribute almost equally to the DOS. Even though Y_8CoIn_3 is composed of metallic elements, covalent bonds are formed between the Y 4d, Co 3d, and In 5p orbitals[42], resulting in a semimetallic DOS. In addition to these atomic orbital states, the bands in the immediate vicinity of the Fermi level also originate from three interstitial states near the Co atoms (Fig. 2d), which are related to each other by the threefold rotational symmetry around the Co atoms.

Along the Γ-A line, there is a little co-group C_{6v}. This group has two distinct 2-dimensional irreps, Δ_5 and Δ_6, which are distinguished by eigenvalues of the screw symmetry around the z-axis. This situation is similar to a benzene molecule with C_{6v}, where the highest occupied molecular orbital and lowest unoccupied molecular orbital have double degeneracy of different irreps. By contrast, C_{3v} and C_{4v} symmetries cannot have two distinct types of 2-dimensional irreps in spinless systems. The two bands that intersect along the Γ-A line belong to the two different 2-dimensional irreps Δ_5 and Δ_6 (Fig. 2a). These bands cannot hybridize, and their crossing points are fourfold degenerate Dirac points (without counting the spin degeneracy). When the SOC is turned on, the system becomes a spinful Dirac semimetal. The SOC's magnitude at the Dirac point can be adjusted from 20 meV to 75 meV through the elemental substitutions (see "Spinful Dirac semimetal" Section and Supplementary Note 3).

Figure 2e shows the 3-dimensional picture of the band structure around the Dirac point in the $k_x = 0$ plane, calculated without the SOC. We see that the band dispersion around the Dirac point is linear in all directions. As already mentioned, both the valence and the conduction bands are doubly degenerate on the k_z-axis (Γ-A line), which is indicated by the black lines in Fig. 2e. These degeneracies are lifted away from the k_z-axis. To see this, we construct a low-energy 4×4 $k \cdot p$ Hamiltonian up to the second order in k around the Dirac point. We find that the two-fold degenerate valence and conduction bands split into four bands, except along the nodal lines marked in white in Fig. 2e, where either valence or conduction band is two-fold degenerate; we will discuss these nodal lines in more detail below. These features are different from the band structure of spinful Dirac semimetals with spatial inversion symmetry, such as Na_3Bi, where the bands are Kramers degenerate throughout the BZ.

Next, we discuss the topological invariants that characterize the bulk states of Y_8CoIn_3. The Zak phase along the x-axis

$$\theta(k_y, k_z) = -\mathrm{i}\sum_n^{\mathrm{occ.}} \oint dk_x \langle u_n(\mathbf{k})| \frac{\partial}{\partial k_x} |u_n(\mathbf{k})\rangle \quad (1)$$

is quantized to either 0 or π (mod 2π) due to the mirror symmetry about the yz-plane. This means that the Wannier functions are located at mirror-symmetric positions. We find that the nontrivial topology of the bulk states of Y_8CoIn_3 is characterized by the Zak phase $\theta(0, k_z)$ calculated in the $k_y = 0$ plane. The $k_y = 0$ plane is invariant under the glide operation with respect to the zx-plane, and the wavefunctions in this plane can be chosen to be

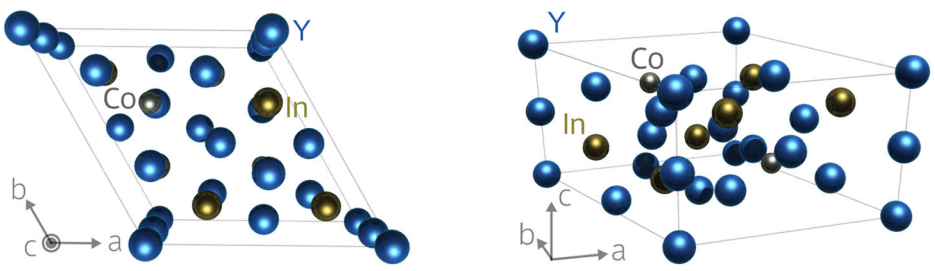

Fig. 1 | Crystal structure of Y_8CoIn_3. The blue, gray, and gold balls represent Y, Co, and In atoms, respectively.

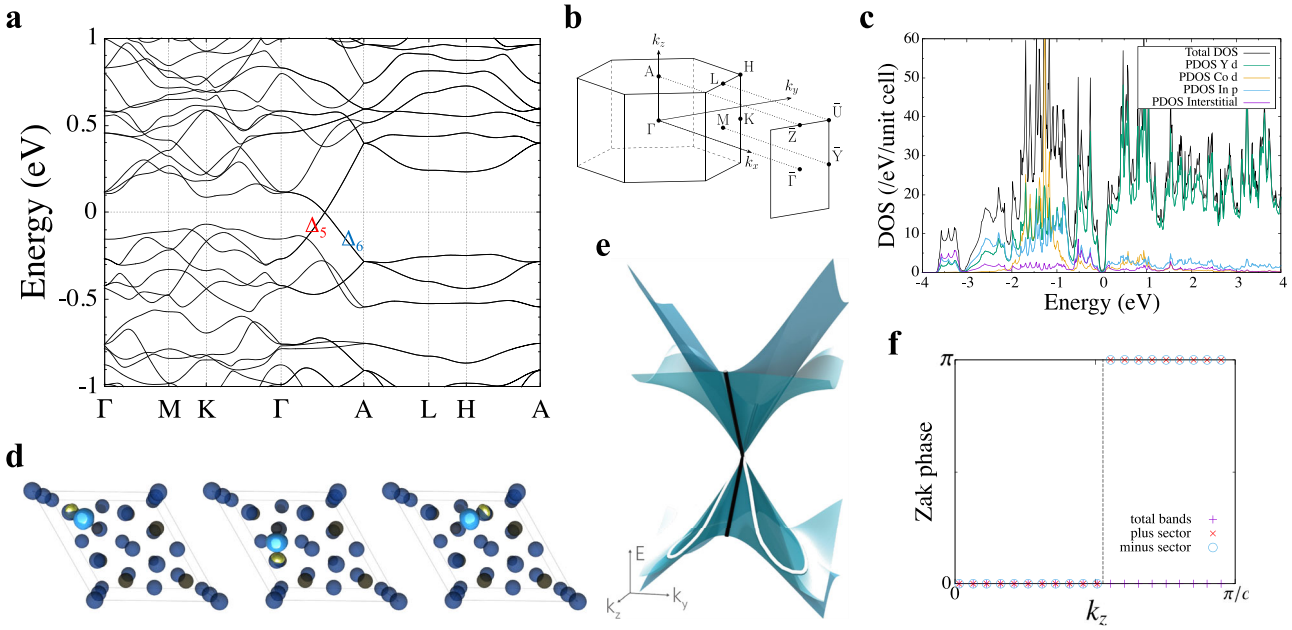

Fig. 2 | The electronic structure of Y_8CoIn_3 calculated without the SOC. a The electronic band structure of Y_8CoIn_3 calculated by the generalized gradient approximation (GGA). The irreps of the two bands forming the Dirac point in the Γ-A line are shown. The energy is measured from the Fermi level. **b** The bulk BZ and the projected surface BZ for the (1000) surface. **c** The total and partial density of states (PDOS) calculated with the Wannier functions. **d** The interstitial Wannier functions near the Co atoms. The differently colored surfaces represent isosurfaces of opposite signs. **e** The 3-dimensional band structure around the Dirac point calculated in the $k_x = 0$ plane. The black (white) lines represent degeneracies between the valence bands or between the conduction bands on (off) the k_z-axis. **f** The Zak phases along the x-axis for each glide sector. The dashed line represents the coordinate of the Dirac point.

eigenstates of the glide operation. We classify the occupied bands in the $k_y = 0$ plane into two sectors according to the sign of the eigenvalues of the glide operation, and calculate the Zak phases for each sector. As shown in Fig. 2f, the Zak phases change from 0 to π at the Dirac point in both sectors. Note that the Zak phases calculated from all occupied bands have no jump of π at the Dirac point, since the sum of the Zak phases for each sector is 0 (mod 2π) at all k_z.

As shown in Fig. 2e, there are lines of degeneracies between two valence bands and between two conduction bands, which are connected to the Dirac point. These nodal lines are found not only on the k_z-axis but also on the mirror or glide planes. Figure 3 shows the color maps of the energy difference between the two highest valence bands and between the two lowest conduction bands of Y_8CoIn_3. The calculations are performed in the mirror invariant plane $k_x = 0$ and the glide invariant plane $k_y = 0$. All four panels show the degeneracy of the bands forming 2-dimensional irreps on the k_z-axis. While no additional band degeneracy is found in the $k_y = 0$ plane (Fig. 3c, d), the two highest valence bands (Fig. 3a) and two lowest conduction bands (Fig. 3b) of Y_8CoIn_3 have nodal lines in the $k_x = 0$ plane extending from the Dirac point ($k_z^{\mathrm{D}} \simeq 0.237$ Å^{-1}) to the diagonal directions, $k_z > k_z^{\mathrm{D}}$ in a and $k_z < k_z^{\mathrm{D}}$ in b.

These properties are explained using the effective $k \cdot p$ Hamiltonian expanded around the Dirac point up to the second order in k. The effective Hamiltonian has the form

$$\begin{aligned} H(\mathbf{k}) = {} & c_1 k_z \Gamma_{0,0} + c_2 k_z \Gamma_{3,0} + c_3 (k_x \Gamma_{2,0} - k_y \Gamma_{1,2}) \\ & + c_4 (k_x \Gamma_{1,0} + k_y \Gamma_{2,2}) + c_5 (k_x^2 + k_y^2) \Gamma_{0,0} \\ & + c_6 k_z^2 \Gamma_{0,0} + c_7 [(k_x^2 - k_y^2) \Gamma_{3,3} - 2 k_x k_y \Gamma_{0,1}] \\ & + c_8 (k_x k_z \Gamma_{2,0} - k_y k_z \Gamma_{1,2}) + c_9 (k_x k_z \Gamma_{1,0} + k_y k_z \Gamma_{2,2}) \\ & + c_{10} (k_x^2 + k_y^2) \Gamma_{3,0} + c_{11} k_z^2 \Gamma_{3,0} \\ & + c_{12} [(k_x^2 - k_y^2) \Gamma_{0,3} - 2 k_x k_y \Gamma_{3,1}], \end{aligned} \tag{2}$$

where the Γ matrices are the direct products of the Pauli matrices σ_i ($i = 1, 2, 3$) and a 2×2 unit matrix σ_0, i.e., $\Gamma_{i,j} = \sigma_i \otimes \sigma_j$. This Hamiltonian has a sixfold rotational symmetry around the z-axis $D(C_{6z}) H(\mathbf{k}) D(C_{6z})^\dagger = H(C_{6z}\mathbf{k})$ [$D(C_{6z}) = -(\Gamma_{3,0} + \mathrm{i}\sqrt{3}\Gamma_{0,2})/2$] , and a mirror symmetry about the zx-plane $D(M_y) H(\mathbf{k}) D(M_y)^\dagger = H(M_y\mathbf{k})$ [$D(M_y) = \Gamma_{0,3}$], hence it has C_{6v} symmetry. Note that a previous study[38] has also systematically constructed the $k \cdot p$ theory in *linear order* in k, whereas our Hamiltonian in Eq. (2) takes into account the *second-order* terms that are crucial for the following discussions. The band structure obtained by first-principles calculations is well fitted in the neighborhood of the Dirac point by the Hamiltonian in Eq. (2), and the obtained parameters are presented in Supplementary Note 4. The eigenvalues of $H(\mathbf{k})$ in the $k_x = 0$ plane are

$$\begin{aligned} E(0, k_y, k_z) = {} & [c_5 + (-1)^{s_1} c_7] k_y^2 + (c_1 + c_6 k_z) k_z \\ & + (-1)^{s_2} \Big\{ (c_3 + c_8 k_z)^2 k_y^2 + (c_4 + c_9 k_z)^2 k_y^2 \\ & + \Big[c_2 k_z + c_{10} k_y^2 + (-1)^{s_1} c_{12} k_y^2 + c_{11} k_z^2 \Big]^2 \Big\}^{1/2}, \end{aligned} \tag{3}$$

where $s_1, s_2 \in \{0, 1\}$. The valence bands ($s_2 = 1$) are degenerate at $k_y \neq 0$, when the condition

$$c_7 \sqrt{(c_3^2 + c_4^2) k_y^2 + c_2^2 k_z^2} = c_2 c_{12} k_z \tag{4}$$

is satisfied in the leading order of k. By squaring both sides we obtain

$$c_7^2 (c_3^2 + c_4^2) k_y^2 = c_2^2 (c_{12}^2 - c_7^2) k_z^2. \tag{5}$$

Therefore, when $|c_{12}| > |c_7|$, the valence bands are degenerate along the straight lines $k_z \propto \pm k_y$ emanating from the Dirac point. Note that, according to Eq. (4), the degeneracies occur only in the part of the lines described by Eq. (5) that satisfies $c_2 c_7 c_{12} k_z > 0$. Similarly, when $|c_{12}| > |c_7|$, the conduction bands are degenerate in the part of the lines represented by Eq. (5) that satisfies $c_2 c_7 c_{12} k_z < 0$. On the other hand, when $|c_7| > |c_{12}|$, the valence bands

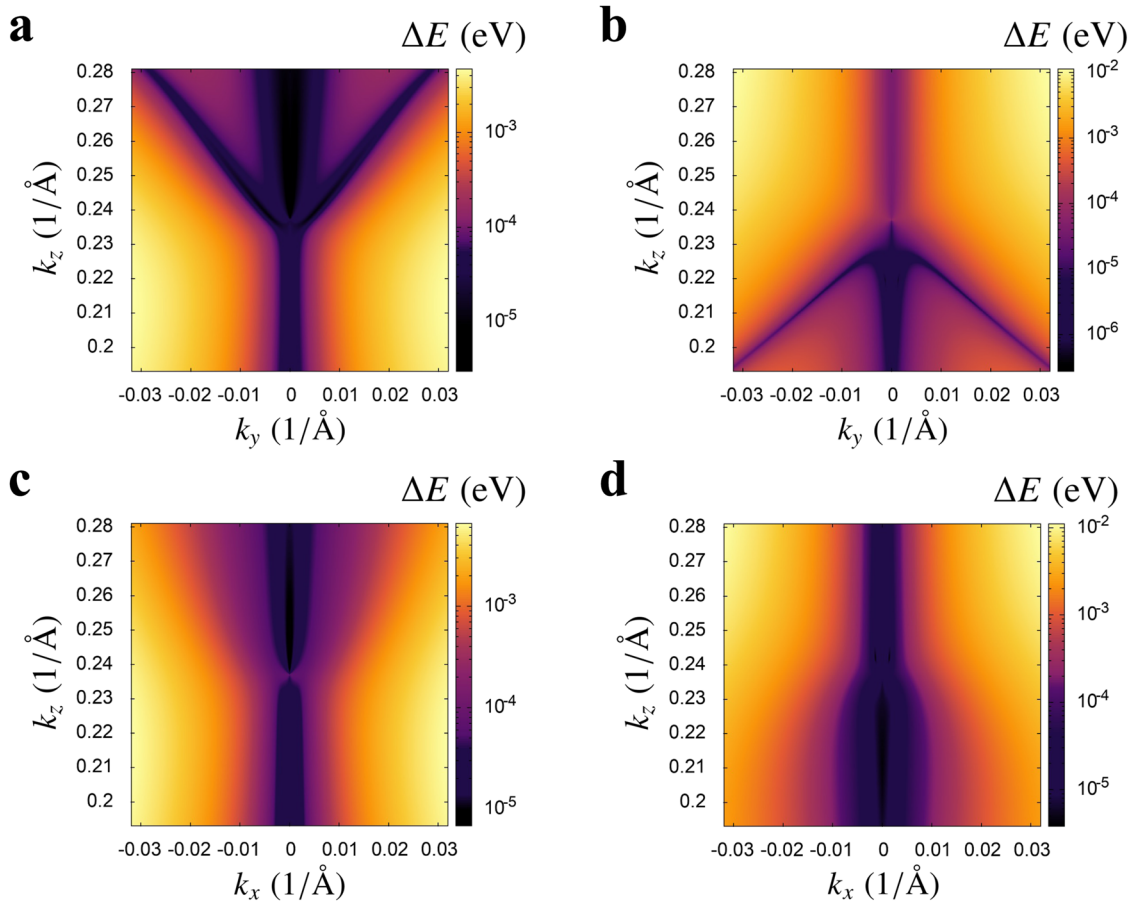

Fig. 3 | Color maps of the energy difference with logarithmic scale. The energy difference between the two topmost valence bands and between the two bottommost conduction bands of Y_8CoIn_3 on the mirror invariant plane $k_x = 0$ are shown in (**a**) and (**b**), respectively. The energy difference between the two topmost valence bands and between the two bottommost conduction bands on the glide invariant plane $k_y = 0$ are shown in (**c**) and (**d**), respectively.

and the conduction bands on the $k_y = 0$ plane are degenerate in the part of the lines represented by

$$c_{12}^2(c_3^2 + c_4^2)k_x^2 = c_2^2(c_7^2 - c_{12}^2)k_z^2 \tag{6}$$

that satisfies $c_2c_7c_{12}k_z > 0$ and $c_2c_7c_{12}k_z < 0$, respectively. We note that $0 < c_2 < c_7 < c_{12}$ in Y_8CoIn_3. From the above discussion, we conclude that in the spinless Dirac semimetal phase protected by C_{6v} symmetry, both the valence bands and the conduction bands are degenerate along the straight lines passing through the Dirac point extending to the opposite directions to each other on one of the two equivalent mirror invariant planes determined by the relative magnitude of c_7 and c_{12}.

Surface states

We calculate the surface states for the (1000) surface of Y_8CoIn_3, using the surface termination shown in Fig. 4a and the surface BZ shown in Fig 2b. As shown in Fig. 4b, two nontrivial surface bands emerge from the projection of the bulk Dirac point. The absence or presence of the nontrivial surface bands in the $\bar{\Gamma}$-$\bar{Z}$ line corresponds to the Zak phase values of 0 or π, respectively. Also, the number of nontrivial surface bands corresponds to the number of glide sectors for which the Zak phase is π. This correspondence between the Zak phases for each sector and the nontrivial surface bands are reproduced by the 4×4 tight-binding model with the C_{6v} point group symmetry and time-reversal symmetry, as described in Supplementary Note 5.

The crystal maintains the glide symmetry with respect to the zx-plane when the surface is in this direction. The $\bar{Z}$-$\bar{U}$ line is invariant up to the reciprocal lattice vector under the product of the glide operation $\{M_y|00\frac{1}{2}\}$ and the time reversal operation Θ. The product $\{M_y|00\frac{1}{2}\}\Theta$ is an anti-unitary operator and $(\{M_y|00\frac{1}{2}\}\Theta)^2$ is -1 when $ck_z = \pi$; therefore the Kramers-like degeneracy occurs on the $\bar{Z}$-$\bar{U}$ line. This explains the degeneracy of the two midgap surface states along the $\bar{Z}$-$\bar{U}$ line.

The second SW class

From this section onwards, we investigate phase transitions exhibited by the spinless Dirac semimetal phase, which is located at phase boundaries of various topological phases. First, we explore phase transitions in the spinless systems. By applying uniaxial pressure to Y_8CoIn_3, we can transform it into a multi-band nodal-line or Weyl semimetallic phase characterized by the second SW class.

In the space group $P6_3mc$, the $k_z = 0$ plane is invariant under the product of the twofold screw operation $\{C_{2z}|00\frac{1}{2}\}$ and the time reversal operation Θ. Since $\{C_{2z}|00\frac{1}{2}\}\Theta$ is an anti-unitary operator and satisfies $(\{C_{2z}|00\frac{1}{2}\}\Theta)^2 = +1$ in the $k_z = 0$ plane, we can adopt the real gauge for the wavefunctions in the $k_z = 0$ plane. Recalling that Y_8CoIn_3 has a finite energy gap throughout the $k_z = 0$ plane, the Hamiltonian on this plane is topologically characterized by a $\mathbb{Z}_2$ invariant called the second SW class[25,43–47]. The second SW class w_2 can be obtained by the Wilson loop method[46–50]. Figure 5a shows the Wilson loop spectrum of Y_8CoIn_3 calculated in the $k_z = 0$ plane, where the integral path of the Wilson loop is along the k_x direction at fixed k_y. The spectrum has one linear crossing at π, indicating $w_2 = 1$ in this plane. On the other hand, in the $k_z = \pi/c$ plane, $(\{C_{2z}|00\frac{1}{2}\}\Theta)^2$ is -1 instead of $+1$. In this case, the second homotopy group of the corresponding classifying space is the trivial group and gapped Hamiltonians have no topological distinction[25].

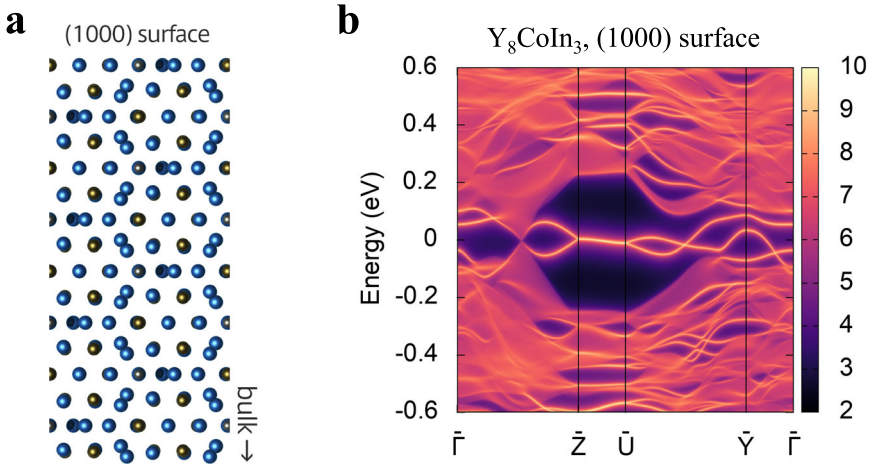

Fig. 4 | Surface states in Y_8CoIn_3. **a** The surface termination used in the calculation. **b** The surface states for the (1000) surface.

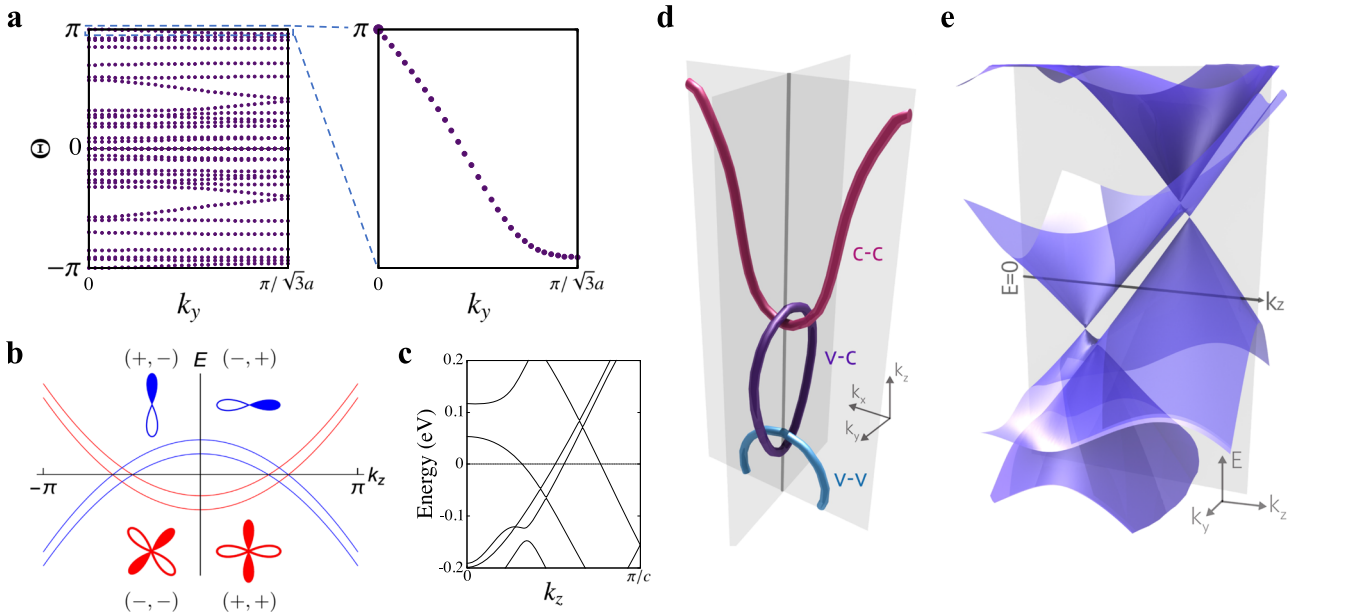

Fig. 5 | The second SW class and the topological phase transitions of Y_8CoIn_3. **a** The Wilson loop spectrum of Y_8CoIn_3 calculated in the $k_z = 0$ plane. The integral path of the Wilson loop is along the k_x direction at fixed k_y. **b** Schematic band structure of C_{2z} and Θ symmetric systems with different second SW classes in the $k_z = 0$ and $k_z = \pi$ planes. The colors of the bands, red and blue, correspond to the C_{2z} eigenvalue values, + and −, respectively. The atomic orbital-like bases and their mirror eigenvalues (eigenvalues for M_x and for M_y in this order) are also written for the case of C_{2v} symmetry. In this case, the degeneracies between a red band and a blue band occur on either the $k_x = 0$ plane or the $k_y = 0$ plane. **c** The band structure on the k_z-axis of Y_8CoIn_3 compressed by 5% in the x direction. **d** The nodal structure of Y_8CoIn_3 compressed by 5% in the x direction. The nodal line between the valence and conduction bands is drawn in purple, and the nodal line between the two highest valence bands (lowest conduction bands) is drawn in blue (red). The gray planes represent the $k_x = 0$ and $k_y = 0$ planes. **e** The 3-dimensional band structure in the $k_x = 0$ plane of Y_8CoIn_3 compressed by 5% in the direction making an angle of $\pi/4$ from the x-axis. The gray plane shows the k_z-E plane at $k_y = 0$.

In fact, when the system has both C_{2z} (or screw) and Θ symmetries, w_2 can be determined from the C_{2z} eigenvalues as follows[43,46]:

$$(-1)^{w_2} = \prod_{i=1}^{4} (-1)^{\lfloor N^-_{\rm occ}(\Gamma_i)/2 \rfloor}, \tag{7}$$

where $\{\Gamma_i\}$ are the C_{2z} invariant points on the plane where w_2 is evaluated, $N^-_{\rm occ}(\Gamma_i)$ is the number of occupied bands with negative C_{2z} eigenvalues at Γ_i, and $\lfloor \cdot \rfloor$ represents the floor function. From this formula, it can be seen that for symmorphic systems with C_{2z} and Θ symmetries, when the w_2 indices in the $k_z = 0$ and $k_z = \pi$ planes are different, two band inversions occur between bands with different C_{2z} eigenvalues as shown in Fig. 5b, which is called a double band inversion. In this case, four bands form a gap-closing object in $0 < k_z < \pi$, which mediates the two planes with different w_2. In Y_8CoIn_3, the two 2-dimensional irreps Δ_5 and Δ_6, which are distinguished by the twofold screw eigenvalues, intersect on the k_z-axis, similarly to the band structure in Fig. 5b. Although w_2 cannot be defined on the $k_z = \pi$ plane in Y_8CoIn_3, the Dirac point can be considered to act as an intermediary between the $k_z = 0$ plane hosting the nontrivial w_2 and the $k_z = \pi$ plane having the trivial topology.

The C_{6v} symmetry is actually not required for the definition of w_2 and its calculation from the C_{2z} eigenvalues. We thus investigate the topological phase transitions of Y_8CoIn_3 under uniaxial strains that break C_{6v} symmetry but maintain C_2 symmetry. Compressing the Y_8CoIn_3 lattice by 5% in the x direction results in space group $Cmc2_1$ (no. 36), and its little co-group on the k_z-axis is C_{2v}. Figure 5c shows the band structure calculated on the k_z-axis, where the 2-dimensional irreps are split due to the symmetry reduction. Since the twofold screw eigenvalues of the occupied bands in the $k_z = 0$ plane remain unchanged, w_2 is invariant. However, in this system, a nodal line on the mirror invariant plane $k_x = 0$ mediates the $k_z = 0$ and $k_z = \pi$ planes

instead of the Dirac point. Furthermore, in this system, nodal lines between the two highest valence bands and between the two lowest conduction bands lie on the glide invariant plane $k_y = 0$ and pass inside the nodal line between the valence and conduction bands as shown in Fig. 5d. The fact that the nodal lines appear on the two different mirror-invariant planes can be understood from the symmetry of the bands. For example, a band with the d_{xy} orbital symmetry can intersect a band with the p_x orbital symmetry in the $k_y = 0$ plane, whereas it can intersect a band with the p_y orbital symmetry in the $k_x = 0$ plane (see Fig. 5b). Notably, wavefunctions with positive (negative) C_2 eigenvalues have the same (different) eigenvalues for the two orthogonal mirror reflections.

We analyze this system using the $k \cdot p$ Hamiltonian in Eq. (2). The k-independent perturbation that breaks C_{6v} but preserves C_{2v} symmetry has the form $c_{13}\Gamma_{0,3} + c_{14}\Gamma_{3,3}$. In the following, we investigate the nodal lines near $\mathbf{k} = \mathbf{0}$ in the leading order of k, assuming that the perturbation is sufficiently small. First, let $c_{13} = 0$ for simplicity. Then, the eigenvalues on the $k_x = 0$ plane are

$$\begin{aligned} E(0, k_y, k_z) = &-(-1)^{s_1} c_{14} + [c_5 + (-1)^{s_1} c_7]k_y^2 + (c_1 + c_6 k_z)k_z \\ &+ (-1)^{s_2}\Big\{(c_3 + c_8 k_z)^2 k_y^2 + (c_4 + c_9 k_z)^2 k_y^2 \\ &+ \Big[c_2 k_z + c_{10} k_y^2 + (-1)^{s_1} c_{12} k_y^2 + c_{11} k_z^2\Big]^2\Big\}^{1/2}, \end{aligned} \tag{8}$$

where $s_1, s_2 \in \{0, 1\}$, and the top valence and bottom conduction bands are degenerate along the curve defined by

$$(c_3^2 + c_4^2 + 2c_7 c_{14})k_y^2 + c_2^2 k_z^2 = c_{14}^2. \tag{9}$$

Since the perturbation c_{14} is assumed to be small, this represents an ellipse around $\mathbf{k} = \mathbf{0}$. We note that this nodal ring cannot be gapped out by tuning c_{14}. Suppose we start from the nodal-line semimetal phase and change c_{14} through 0. As c_{14} approaches 0, the size of the nodal ring decreases. At $c_{14} = 0$ the nodal ring shrinks to the Dirac point, but when c_{14} becomes finite after the sign reversal, it grows into a nodal ring again.

Similarly, on the $k_y = 0$ plane, the two valence bands and also the two conduction bands are degenerate along

$$[c_{10} \pm \mathrm{sgn}(c_{14})c_{12}]k_x^2 + c_2 k_z = 0, \tag{10}$$

where $\pm$ corresponds to the valence and conduction bands, respectively, and $\mathrm{sgn}(\cdot)$ denotes the sign function. The degenerate $\mathbf{k}$ points form two parabolas with the vertex at $\mathbf{k} = \mathbf{0}$ and thread the nodal line defined by Eq. (9). These features coincide with those of nodal lines with $\mathbb{Z}_2$ monopole charge in PT-symmetric systems[23,46], where PT is the product of space inversion and time reversal operators. However, it should be noted that our system does not have space inversion symmetry, but has C_{2v} symmetry instead. In the general case with $c_{13} \neq 0$, the planes where the nodal lines emerge switch between the $k_x = 0$ and $k_y = 0$ planes depending on the relative magnitude of c_{13} and c_{14}, and the two connected parabolas of Eq. (10) are turned into two branches of a hyperbola as shown in Fig. 5d. The details of the calculations are presented in Supplementary Note 6. Note that, depending on the sign of the perturbation parameters, the degeneracies between the valence bands and between the conduction bands represented by Eqs. (5) and (6) can remain in the plane, but shift enough from the k_z-axis to move outside of the nodal ring in Eq. (9).

When the system is compressed in the direction with an angle of $\pi/4$ from the x-axis, the space group transforms into $P2_1$ (no. 4), and its little co-group on the k_z-axis becomes C_2. Under this distortion, the $k_z = 0$ plane still preserves the nontrivial w_2. However, the gap-closing object bridging the $k_z = 0$ and $k_z = \pi$ planes becomes a pair of Weyl points with opposite chirality (Fig. 5e). This phenomenon is typical of Dirac semimetal phases with broken spatial inversion symmetry and has been discussed in previous studies[51–54]. The analytical argument with the $k \cdot p$ Hamiltonian is given in Supplementary Note 7.

The results of the second SW class for the Dirac, nodal-line, and Weyl semimetals are combined as follows. The gapped Hamiltonian in the $k_z = 0$ plane of nonsymmorphic systems with $\{C_{2z}|00\frac{1}{2}\}$ and Θ is characterized by the second SW class w_2, which takes the $\mathbb{Z}_2$ values. If $w_2 = 1$ and the system has a finite energy gap except on the k_z-axis, a gap-closing object is formed by four bands on the k_z-axis. Depending on the symmetry, it can be a pair of Weyl points, a nodal line, or a Dirac point. This is also the case for symmorphic systems with different w_2 on the $k_z = 0$ and $k_z = \pi$ planes. In this perspective, the Dirac semimetal such as Y_8CoIn_3 can be understood as a system with a double band inversion where the parameters are fine-tuned by the symmetry. The surface states of the three topological semimetal phases characterized by the second SW class are discussed in Supplementary Note 8.

Spinful Dirac semimetal

We now turn our attention to the spinful systems. Since Y_8CoIn_3 is mostly composed of Y, strong SOC can be introduced by substitution to lanthanides. Figure 6a shows the electronic band structure of Lu_8CoGa_3 calculated in the presence and absence of the SOC. The Lu 5d orbitals have a strong SOC compared to the Y 4d orbitals, resulting in significant SOC splitting near the Fermi level in Lu_8CoGa_3. In Fig. 6b, the single-valued representations Δ_5 and Δ_6 transform into $\Delta_7 \oplus \Delta_8$ and $\Delta_7 \oplus \Delta_9$, respectively, when the SOC is turned on. The double-valued representations Δ_7, Δ_8, and Δ_9 are

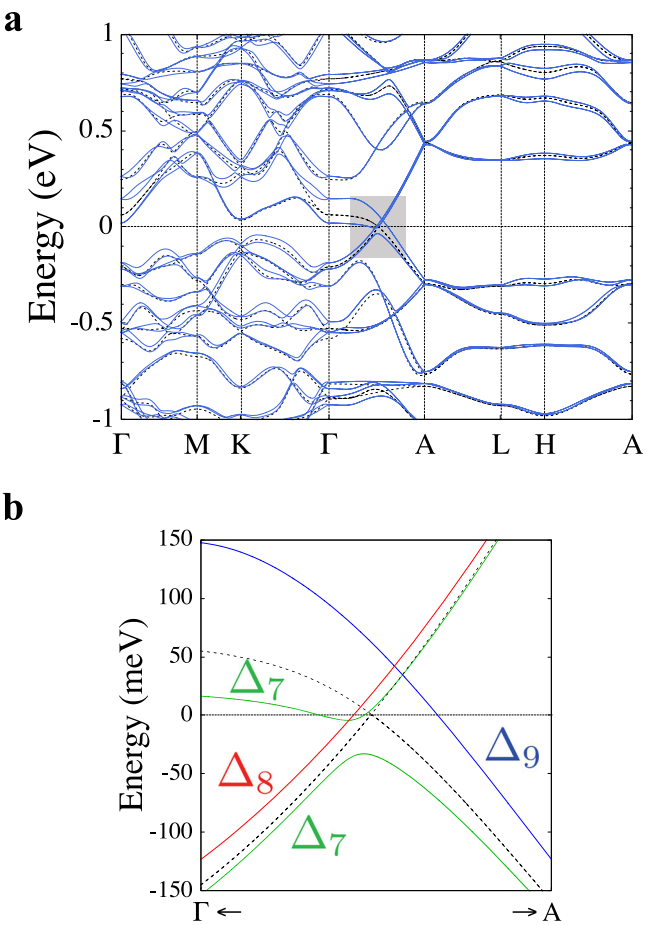

Fig. 6 | The electronic band structure of Lu_8CoGa_3 calculated with and without the SOC. a The electronic band structure of Lu_8CoGa_3 calculated by the GGA. The blue solid line and the black dashed line show the result with and without the SOC, respectively. The energy is measured from the Fermi level in the spinless calculation. **b** Magnified band structure in the shaded region in (**a**). The irreps of the bands with the SOC are indicated.

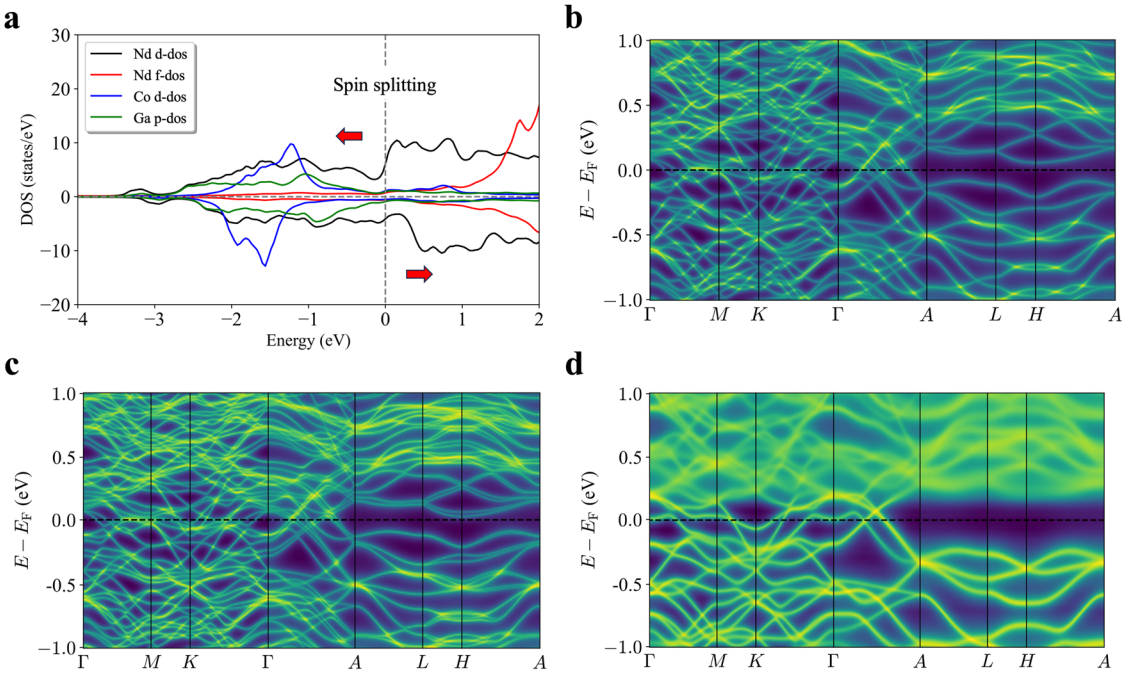

Fig. 7 | The electronic structure of the magnetic material Nd_8CoGa_3 calculated by the KKR method. a The PDOS of Nd_8CoGa_3 calculated without the SOC. **b** The electronic band structure of Nd_8CoGa_3 without the SOC. **c** The electronic band structure of Nd_8CoGa_3 with the SOC included self-consistently in ferromagnetic configurations. **d** The electronic band structure of Nd_8CoGa_3 in the paramagnetic state computed using the DLM approach. The smearing of the bands is due to the finite temperature effects.

all 2-dimensional irreps that are distinguished by the screw symmetry around the z-axis. The two bands belonging to Δ_7 hybridize and open the energy gap. The hybridization of bands belonging to different representations is prohibited; therefore, three Dirac points are formed near the Fermi level, which are not related by any symmetry and have different energies. The SOC gap of Lu_8CoGa_3 can be measured by taking the energy difference between the maximum of the lower Δ_7 band and the intersection of the Δ_8 and Δ_9 bands, which approximately equals 75 meV. When Lu is replaced with Y, the magnitude of the SOC is drastically reduced to 1/3 or less (see Supplementary Note 3).

Magnetic Weyl semimetal

The use of lanthanides as substitutes can introduce magnetism. In the presence of magnetic rare-earth atoms, the time-reversal symmetry is broken. It is intriguing to examine the evolution of topological features near the Fermi energy in the presence of a finite magnetization. The Dirac cone is expected to split into a pair of Weyl points with opposing chiralities[1,9,14]. We have opted for Nd_8CoGa_3 as our magnetic prototype system, applying an all-electron full-potential KKR Green function method with the generalized gradient approximation (GGA) for exchange-correlation energy[55]. The nonmagnetic La_8CoGa_3 has a small Fermi surface around the $k_z = 0$ plane (see Supplementary Note 3), and there is also a low DOS at the Fermi level when Nd replaces La (Fig. 7a). The Nd magnetic atom is in a 3 + state, and has a magnetic moment of 3.19 μ_B per atom in agreement with Hund's rules (the moment points along the c-axis). Due to the finite spin polarization on Nd, an induced moment of 0.43 μ_B emerges on the Co atoms with an antiferromagnetic coupling to the Nd atoms. Additionally, a weak induced moment of 0.04 μ_B appears on the Ga atoms.

The electronic band structure for Nd_8CoGa_3 without the SOC is shown in Fig. 7b. As expected from the DOS, the gap is populated by the Co 3*d* and Ga 4*p* bands, as a consequence of the spin splitting introduced by the Nd magnetic moment (see Fig. 7a). Nonetheless, the gap remains open and unaltered along the [AL, LH, HA] directions. This is because a large energy gap is opened around the $k_z = \pi$ plane in RE_8CoX_3 materials, and the number of occupied bands in the magnetic state, excluding the 4*f* orbitals, is unchanged compared to the nonmagnetic state. The band structure for each spin component is presented in Supplementary Note 9. Each of the Dirac points in the Γ-A line splits into a pair of Weyl points in the presence of the SOC as shown in Fig. 7c. Furthermore, given that the filling of the gap originates from the induced spin polarization on Co and Ga, we investigate the electronic band structure in the paramagnetic phase. To simulate the paramagnetic state, we employ the disordered local moment (DLM) approach[56], the fully magnetic disordered state is then established using the coherent potential approximation (CPA)[57]. In the disordered state, the induced moments on the Co and Ga vanish, hence fewer bands are observed in the gap in comparison with the ferromagnetic state (see Fig. 7d). The magnetic disorder causes the smearing of the electronic bands. The dependence of bands populating the gap on the induced spin polarization indicates that the Fermi surface, and semimetallic character can be tuned via the magnetic order and finite temperature effects. Since the spin splitting of itinerant 4*d* electrons is small, the band structure shown in Fig. 7d is in good agreement with the band structure calculated with a pseudopotential that treats the Nd 4*f* orbitals as core states (see Supplementary Note 9). Lastly, as the magnetic order alters the topological band structure of Nd_8CoGa_3, we performed a preliminary analysis of the magnetic interactions in real space using the infinitesimal rotation method[58], and find that the intralayer and interlayer magnetic coupling is predominantly ferromagnetic with a transition temperature of $T_c = 40$ K. The relatively high temperature can be attributed to the high number of rare-earth atoms within the unit cell.

Discussion

In summary, the ternary compounds RE_8CoX_3 (RE = rare earth elements, X = Al, Ga, or In) are the ideal platform for the spinless Dirac semimetal and the topological transitions. The strength of the SOC in these materials can be adjusted by substituting elements, and those containing Y have a smaller SOC. The Dirac points in these materials are manifested by accidental degeneracy of the two different 2-dimensional irreps of C_{6v} on the k_z-axis. The degeneracies between the valence bands and between the conduction bands are generally lifted away from the k_z-axis, but there are degenerate lines on the mirror planes extending from the Dirac points. The nontrivial topology of the bulk states is characterized by the Zak phases for each glide sector, which corresponds to the two midgap bands in the surface extending

from the projection of the bulk Dirac point. Furthermore, we discuss the topological phase transitions under the distortions and the elemental substitutions. Uniaxial compression, which preserves the twofold screw symmetry, breaks the C_{6v} symmetry and turns the Dirac point into the nodal line or the pair of Weyl points. The magnetic lanthanide elements can replace Y, resulting in a spinful magnetic Weyl semimetallic phase in the system.

Methods

The electronic structure of Y_8CoIn_3 is calculated based on density functional theory (DFT) as implemented in the Vienna Ab initio Simulation Package[59]. For the exchange-correlation function, we employ the GGA of Perdew, Burke, and Ernzerhof (PBE)[60]. The cutoff energy for the plane wave expansion is 350 eV and a k-point mesh of $8 \times 8 \times 12$ is adopted. The calculations are based on the experimental crystal structure. The irreps of the bands are obtained using the IrRep package[61,62]. To calculate the PDOS, Zak phases, and surface states, we construct a tight-binding Hamiltonian from the DFT results using the Wannier90 package[63]. From the Bloch functions within the range from 4 eV below to 10 eV above the Fermi level, we construct 114 Wannier functions for the Y 4*d* orbitals, the Co 3*d* orbitals, the In 5*p* orbitals, and the interstitial *s* orbitals near the Co atoms. The surface states are calculated by the iterative Green's function method[64–66] implemented in the WannierTools package[67]. The WannierTools package is also used, *mutatis mutandis*, to calculate the Zak phases. When we investigate topological phase transitions caused by uniaxial strains, the lattice is compressed in one direction and expanded uniformly in the two orthogonal directions so that the volume of the unit cell is preserved, and then the structure is optimized using the revised PBE for solids[68] as the exchange-correlation functional.

For the magnetic Weyl semimetals, our first-principles simulations employ the all-electron full-potential KKR Green function method[69] with and without SOC. The 4*f* electrons are treated using the DFT + U approach in the Dudarev formulation[70] with $U = 6$ eV. The self-consistent energy contour is divided into 48 energy points with a $25 \times 25 \times 25$ k-mesh in the BZ. The electronic band structure along the high symmetry path represents the quasiparticle density of states computed directly from the Green function in the ordered ferromagnetic or paramagnetic (DLM) states[71].

Data availability

The datasets generated and analyzed during the current study are available from the corresponding author upon reasonable request.

Received: 13 February 2024; Accepted: 9 September 2024;
Published online: 15 November 2024

References

1. Armitage, N. P., Mele, E. J. & Vishwanath, A. Weyl and Dirac semimetals in three-dimensional solids. *Rev. Mod. Phys.* **90**, 015001 (2018).
2. Xu, S.-Y. et al. Discovery of a Weyl fermion state with Fermi arcs in niobium arsenide. *Nat. Phys.* **11**, 748 (2015).
3. Yang, L. X. et al. Weyl semimetal phase in the non-centrosymmetric compound TaAs. *Nat. Phys.* **11**, 728 (2015).
4. Lv, B. Q. et al. Experimental discovery of Weyl semimetal TaAs. *Phys. Rev. X* **5**, 031013 (2015).
5. Weng, H., Fang, C., Fang, Z., Bernevig, B. A. & Dai, X. Weyl semimetal phase in noncentrosymmetric transition-metal monophosphides. *Phys. Rev. X* **5**, 011029 (2015).
6. Hirayama, M., Okugawa, R., Ishibashi, S., Murakami, S. & Miyake, T. Weyl node and spin texture in trigonal tellurium and selenium. *Phys. Rev. Lett.* **114**, 206401 (2015).
7. Young, S. M. et al. Dirac semimetal in three dimensions. *Phys. Rev. Lett.* **108**, 140405 (2012).
8. Liu, Z. K. et al. Discovery of a three-dimensional topological Dirac semimetal, Na_3Bi. *Science* **343**, 864 (2014).
9. Wang, Z. et al. Dirac semimetal and topological phase transitions in A_3Bi (A = Na, K, Rb). *Phys. Rev. B* **85**, 195320 (2012).
10. Neupane, M. et al. Observation of a three-dimensional topological Dirac semimetal phase in high-mobility Cd_3As_2. *Nat. Commun.* **5**, 3786 (2014).
11. Liu, Z. K. et al. A stable three-dimensional topological Dirac semimetal Cd_3As_2. *Nat. Mater.* **13**, 677 (2014).
12. Jeon, S. et al. Landau quantization and quasiparticle interference in the three-dimensional Dirac semimetal Cd_3As_2. *Nat. Mater.* **13**, 851 (2014).
13. Borisenko, S. et al. Experimental realization of a three-dimensional Dirac semimetal. *Phys. Rev. Lett.* **113**, 027603 (2014).
14. Wang, Z., Weng, H., Wu, Q., Dai, X. & Fang, Z. Three-dimensional Dirac semimetal and quantum transport in Cd_3As_2. *Phys. Rev. B* **88**, 125427 (2013).
15. Kim, Y., Wieder, B. J., Kane, C. L. & Rappe, A. M. Dirac line nodes in inversion-symmetric crystals. *Phys. Rev. Lett.* **115**, 036806 (2015).
16. Yu, R., Weng, H., Fang, Z., Dai, X. & Hu, X. Topological node-line semimetal and Dirac semimetal state in antiperovskite Cu_3PdN. *Phys. Rev. Lett.* **115**, 036807 (2015).
17. Hirayama, M., Okugawa, R., Miyake, T. & Murakami, S. Topological Dirac nodal lines and surface charges in fcc alkaline earth metals. *Nat. Commun.* **8**, 14022 (2017).
18. Takahashi, R., Hirayama, M. & Murakami, S. Spinless hourglass nodal-line semimetals. *Phys. Rev. B* **96**, 155206 (2017).
19. Zhou, F. et al. Pnma metal hydride system LiBH: a superior topological semimetal with the coexistence of twofold and quadruple degenerate topological nodal lines. *J. Phys. Condens. Matter* **32**, 365502 (2020).
20. Carter, J.-M., Shankar, V. V., Zeb, M. A. & Kee, H.-Y. Semimetal and topological insulator in perovskite iridates. *Phys. Rev. B* **85**, 115105 (2012).
21. Zeb, M. A. & Kee, H.-Y. Interplay between spin-orbit coupling and Hubbard interaction in $SrIrO_3$ and related *Pbnm* perovskite oxides. *Phys. Rev. B* **86**, 085149 (2012).
22. Chen, Y., Lu, Y.-M. & Kee, H.-Y. Topological crystalline metal in orthorhombic perovskite iridates. *Nat. Commun.* **6**, 6593 (2015).
23. Fang, C., Chen, Y., Kee, H.-Y. & Fu, L. Topological nodal line semimetals with and without spin-orbital coupling. *Phys. Rev. B* **92**, 081201 (2015).
24. Fang, C., Weng, H., Dai, X. & Fang, Z. Topological nodal line semimetals*. *Chin. Phys. B* **25**, 117106 (2016).
25. Bzdušek, T. & Sigrist, M. Robust doubly charged nodal lines and nodal surfaces in centrosymmetric systems. *Phys. Rev. B* **96**, 155105 (2017).
26. Kruthoff, J., de Boer, J., van Wezel, J., Kane, C. L. & Slager, R.-J. Topological classification of crystalline insulators through band structure combinatorics. *Phys. Rev. X* **7**, 041069 (2017).
27. Po, H. C., Vishwanath, A. & Watanabe, H. Symmetry-based indicators of band topology in the 230 space groups. *Nat. Commun.* **8**, 50 (2017).
28. Bradlyn, B. et al. Topological quantum chemistry. *Nature* **547**, 298 (2017).
29. Tang, F., Po, H. C., Vishwanath, A. & Wan, X. Efficient topological materials discovery using symmetry indicators. *Nat. Phys.* **15**, 470 (2019).
30. Zhang, T. et al. Catalogue of topological electronic materials. *Nature* **566**, 475 (2019).
31. Vergniory, M. G. et al. A complete catalogue of high-quality topological materials. *Nature* **566**, 480 (2019).
32. Tang, F., Po, H. C., Vishwanath, A. & Wan, X. Topological materials discovery by large-order symmetry indicators. *Sci. Adv.* **5**, eaau8725 (2019).
33. Wang, D. et al. Two-dimensional topological materials discovery by symmetry-indicator method. *Phys. Rev. B* **100**, 195108 (2019).
34. Vergniory, M. G. et al. All topological bands of all nonmagnetic stoichiometric materials. *Science* **376**, eabg9094 (2022).

35. Song, Z., Zhang, T. & Fang, C. Diagnosis for nonmagnetic topological semimetals in the absence of spin-orbital coupling. *Phys. Rev. X* **8**, 031069 (2018).
36. Yang, B.-J. & Nagaosa, N. Classification of stable three-dimensional Dirac semimetals with nontrivial topology. *Nat. Commun.* **5**, 4898 (2014).
37. Yang, B.-J., Morimoto, T. & Furusaki, A. Topological charges of three-dimensional Dirac semimetals with rotation symmetry. *Phys. Rev. B* **92**, 165120 (2015).
38. Yu, Z.-M. et al. Encyclopedia of emergent particles in three-dimensional crystals. *Sci. Bull.* **67**, 375 (2022).
39. Dzevenko, M., Hamyk, A., Tyvanchuk, Y. & Kalychak, Y. Phase equilibria in the Er–Co–In system and crystal structure of Er_8CoIn_3 compound. *Open Chem.* **11**, 604 (2013).
40. Dzevenko, M., Bigun, I., Pustovoychenko, M., Havela, L. & Kalychak, Y. Rare-earth rich indides RE_8CoIn_3 (RE = Y, Dy-Tm, Lu). *Intermetallics* **38**, 14 (2013).
41. Grin, Y., Sichevich, O., Gladyshevskii, R. & Yarmolyuk, Y. The crystal structure of the compounds R_8Ga_3Co (R = Ce, Pr, Nd, Sm, Tb, Dy, Ho, Er, Tm). *Kristallografiya* **29**, 708 (1984).
42. Kibria, M. G. & Shattique, M. R. First-principles calculations of electronic, optical and elastic properties of Y_8CoIn_3, in https://doi.org/10.1109/ICEEICT.2014.6919084*2014 International Conference on Electrical Engineering and Information & Communication Technology* pp. 1–4 (2014).
43. Ahn, J. & Yang, B.-J. Symmetry representation approach to topological invariants in $C_{2z}T$-symmetric systems. *Phys. Rev. B* **99**, 235125 (2019).
44. Bouhon, A., Bzdušek, T. & Slager, R.-J. Geometric approach to fragile topology beyond symmetry indicators. *Phys. Rev. B* **102**, 115135 (2020).
45. Kobayashi, S. & Furusaki, A. Fragile topological insulators protected by rotation symmetry without spin-orbit coupling. *Phys. Rev. B* **104**, 195114 (2021).
46. Ahn, J., Kim, D., Kim, Y. & Yang, B.-J. Band topology and linking structure of nodal line semimetals with Z_2 monopole charges. *Phys. Rev. Lett.* **121**, 106403 (2018).
47. Ahn, J., Park, S. & Yang, B.-J. Failure of Nielsen–Ninomiya theorem and fragile topology in two-dimensional systems with space-time inversion symmetry: application to twisted bilayer graphene at magic angle. *Phys. Rev. X* **9**, 021013 (2019).
48. Soluyanov, A. A. & Vanderbilt, D. Computing topological invariants without inversion symmetry. *Phys. Rev. B* **83**, 235401 (2011).
49. Yu, R., Qi, X. L., Bernevig, A., Fang, Z. & Dai, X. Equivalent expression of $\mathbb{Z}_2$ topological invariant for band insulators using the non-Abelian Berry connection. *Phys. Rev. B* **84**, 075119 (2011).
50. Bouhon, A., Black-Schaffer, A. M. & Slager, R.-J. Wilson loop approach to fragile topology of split elementary band representations and topological crystalline insulators with time-reversal symmetry. *Phys. Rev. B* **100**, 195135 (2019).
51. Gao, H., Strockoz, J., Frakulla, M., Venderbos, J. W. F. & Weng, H. Noncentrosymmetric topological Dirac semimetals in three dimensions. *Phys. Rev. B* **103**, 205151 (2021).
52. Gao, H. et al. Dirac–Weyl semimetal: coexistence of Dirac and Weyl fermions in polar hexagonal *ABC* crystals. *Phys. Rev. Lett.* **121**, 106404 (2018).
53. Zhang, T., Hara, D. & Murakami, S. Z_2 Dirac points with topologically protected multihelicoid surface states. *Phys. Rev. Res.* **4**, 033170 (2022).
54. Zhang, T. & Murakami, S. Parallel and anti-parallel helical surface states for topological semimetals. *Sci. Rep.* **13**, 9239 (2023).
55. Perdew, J. P. & Wang, Y. Accurate and simple analytic representation of the electron-gas correlation energy. *Phys. Rev. B* **45**, 13244 (1992).
56. Gyorffy, B. L., Pindor, A. J., Staunton, J., Stocks, G. M. & Winter, H. A first-principles theory of ferromagnetic phase transitions in metals. *J. Phys. F Met. Phys.* **15**, 1337 (1985).
57. Gyorffy, B. L. Coherent-potential approximation for a nonoverlapping-muffin-tin-potential model of random substitutional alloys. *Phys. Rev. B* **5**, 2382 (1972).
58. Liechtenstein, A. I., Katsnelson, M. I. & Gubanov, V. A. Exchange interactions and spin-wave stiffness in ferromagnetic metals. *J. Phys. F Met. Phys.* **14**, L125 (1984).
59. Kresse, G. & Furthmüller, J. Efficient iterative schemes for ab initio total-energy calculations using a plane-wave basis set. *Phys. Rev. B* **54**, 11169 (1996).
60. Perdew, J. P., Burke, K. & Ernzerhof, M. Generalized gradient approximation made simple. *Phys. Rev. Lett.* **77**, 3865 (1996).
61. Iraola, M. et al. IrRep: symmetry eigenvalues and irreducible representations of ab initio band structures. *Comput. Phys. Commun.* **272**, 108226 (2022).
62. Elcoro, L. et al. Double crystallographic groups and their representations on the Bilbao crystallographic server. *J. Appl. Crystallogr.* **50**, 1457 (2017).
63. Pizzi, G. et al. Wannier90 as a community code: new features and applications. *J. Phys. Condens. Matter* **32**, 165902 (2020).
64. Guinea, F., Tejedor, C., Flores, F. & Louis, E. Effective two-dimensional Hamiltonian at surfaces. *Phys. Rev. B* **28**, 4397 (1983).
65. Sancho, M. P. L., Sancho, J. M. L. & Rubio, J. Quick iterative scheme for the calculation of transfer matrices: application to Mo (100). *J. Phys. F Met. Phys.* **14**, 1205 (1984).
66. Sancho, M. P. L., Sancho, J. M. L., Sancho, J. M. L. & Rubio, J. Highly convergent schemes for the calculation of bulk and surface Green functions. *J. Phys. F Met. Phys.* **15**, 851 (1985).
67. Wu, Q., Zhang, S., Song, H.-F., Troyer, M. & Soluyanov, A. A. Wanniertools : an open-source software package for novel topological materials. *Comput. Phys. Commun.* **224**, 405 (2018).
68. Perdew, J. P. et al. Restoring the density-gradient expansion for exchange in solids and surfaces. *Phys. Rev. Lett.* **100**, 136406 (2008).
69. Papanikolaou, N., Zeller, R. & Dederichs, P. Conceptual improvements of the KKR method. *J. Phys. Condens. Matter* **14**, 2799 (2002).
70. Dudarev, S. L. et al. Parametrization of LSDA + U for noncollinear magnetic configurations: multipolar magnetism in UO_2. *Phys. Rev. Mater.* **3**, 083802 (2019).
71. Ebert, H., Koedderitzsch, D. & Minar, J. Calculating condensed matter properties using the KKR-Green's function method-recent developments and applications. *Rep. Prog. Phys.* **74**, 096501 (2011).

Acknowledgements

The authors thank S. Murakami for the valuable discussions. This work was supported by JST CREST (grant no. JPMJCR19T2). M.S. was supported by the Program for Leading Graduate Schools (MERIT-WINGS). S.S. acknowledges financial support from JSPS KAKENHI grants no. 23K13056 and no. 23K03333. S.K. acknowledges financial support from JSPS KAKENHI grants no. 19K14612 and no. 22K03478. M.H. acknowledges financial support from PRESTO, JST (JPMJPR21Q6) and JSPS KAKENHI grants no. 18H03678.

Author contributions

M.H. conceived and designed the project. M.S. performed first-principles calculations for the nonmagnetic materials. J.B. and S.B. studied the magnetic materials, and J.B. conducted first-principles calculations by the KKR method. S.S. constructed the effective model, and M.S., S.S., and A.F. analyzed the model numerically or analytically. M.S., S.S., S.K., I.T., A.F., and M.H. discussed the topological invariants that characterize the system, and M.S. calculated them. M.S., J.B., S.B., A.F., and M.H. wrote the manuscript with contributions from all authors.

Competing interests
The authors declare no competing interests.

Additional information
Supplementary information The online version contains supplementary material available at https://doi.org/10.1038/s43246-024-00635-9.

Correspondence and requests for materials should be addressed to Motoaki Hirayama.

Peer review information *Communications Materials* thanks Tiantian Zhang, Alexander Yaresko, and the other anonymous, reviewer(s) for their contribution to the peer review of this work. Primary Handling Editors: Toru Hirahara and Aldo Isidori.